Research Square

Preprints are preliminary reports that have not undergone peer review.
They should not be considered conclusive, used to inform clinical practice,
or referenced by the media as validated information.

First-Principles Surface Conductivity and Full-Wave Design of γ-Graphyne THz Radiators

Darlan Holanda Cardoso

darlan.cardoso@ananindeua.ufpa.br

Federal University of Para

Igor Ramon Sinimbú Miranda

Federal University of Para

Francisco Aldir Texeira Abreu

Federal University of Para

Miércio Cardoso de Alcântara Neto

Federal University of Para

Carlos Alberto Brito da Silva Jr.

Federal University of Para

Shirsley Joany da Silva dos Santos

Federal University of Para

Jordan Del Nero

Federal University of Para

Research Article

Keywords: Optical Properties, γ-graphyne, Patch Resonator

Posted Date: June 22nd, 2026

DOI: https://doi.org/10.21203/rs.3.rs-9995491/v1

License: This work is licensed under a Creative Commons Attribution 4.0 International License.
Read Full License

Additional Declarations: No competing interests reported.

First-Principles Surface Conductivity and Full-Wave Design of γ-Graphyne THz Radiators

Darlan Holanda Cardoso[1], Igor Ramon Sinimbú Miranda [2,3], Francisco Aldir Texeira Abreu[1], Miércio Cardoso de Alcântara Neto[4], Carlos Alberto Brito da Silva Jr.[5] , Shirsley Joany da Silva dos Santos[5] and Jordan Del Nero[6].

[1] Programa de Pós-Graduação em Engenharia Elétrica, Universidade Federal do Pará, Belém, 66075-110, Brasil

[2] Programa de Pós-Graduação em Física, Universidade Federal do Pará, Belém, 66075-110, Brasil

[3] Departamento de Ciências Naturais, Universidade do Estado do Pará, Castanhal, 68745-000, Brasil

[4] Instituto de Tecnologia, Universidade Federal do Pará, Belém, 66075-110, Brasil

[5] Faculdade de Física, Universidade Federal do Pará, Ananindeua, 67130-660, Brasil

[6] Faculdade de Física, Universidade Federal do Pará, Belém, 66075-110, Brasil

* Corresponding author: darlan.cardoso@ananindeua.ufpa.br

ABSTRACT

We present a first-principles-informed study of terahertz (THz) microstrip patch antennas that use γ-graphyne as the radiating sheet. The complex surface conductivity σ(ω) of γ-graphyne was computed from density functional theory (SIESTA) combined with a Kubo-Greenwood linear-response evaluation and then imported as a dispersive surface boundary into full-wave finite-element (COMSOL) simulations. Four patch topologies are compared: a plain patch (GN), a patch with edge γ-graphyne nanoribbons (GNano), a patch over a photonic-bandgap substrate (GPBG), and a hybrid GNano+PBG design. All designs operate in the low-THz region and exhibit stable resonances with compact electrical size and competitive radiation performance. Key simulated results are: GN and GNano resonate near 3.28–3.29 THz with $-S_{11}$ minima of ≈ −33.6 dB and −34.8 dB and bandwidths of 0.14 THz (fractional BW ≈4.25%); GPBG and GNano+PBG resonate at higher frequencies (≈3.45–3.59 THz) with S_{11} minima between −22 dB and −19.2 dB. Peak broadside gains reach ≈5.9–6.4 dB across the family (GN: 5.94 dB; GPBG: 6.32 dB; GNano: 5.90 dB; GNano+PBG: 6.37 dB) while radiation efficiencies at each design's center frequency lie in the ≈80–83% range. The GNano variant provides the best intrinsic impedance match to 50 Ω (Rin ≈ 51.16 Ω, VSWR ≈ 1.03), furthermore we also calculated the Specific Absorption Rate (SAR). These findings demonstrate that γ-graphyne, when characterized from atomistic theory and applied in device-scale design, is a promising 2D material candidate for compact THz radiators.

Keywords: Optical Properties, *γ-graphyne*, Patch Resonator.

1. Introduction

Terahertz (THz) technology, often defined as the spectral region between 0.1 and 10 THz, lies between the microwave and infrared bands and offers immense potential for next-generation wireless systems. THz waves combine very wide available bandwidths enabling data rates beyond 10 Gbit/s with short wavelengths in the hundreds of micrometers, offering unique capabilities for high-speed communications, high-resolution imaging, and spectroscopy. These attributes make THz attractive for beyond-5G and 6G communications, high-resolution sensing, and material spectroscopy, but they also impose strict requirements on radiating elements because THz propagation suffers from high free-space loss and atmospheric absorption, which demands efficient, low-loss antennas and devices[1–3].

To realize THz links, antenna design must evolve from conventional microwave paradigms. Microstrip patch antennas are ubiquitous at microwave and millimeter-wave frequencies for their low cost and planar integration, but scaling them into the THz band presents challenges. At THz frequencies, the dimensions of a patch (on the order of half-wavelength) become very small (tens of micrometers), and metal losses increase dramatically due to skin effect and plasmonic behavior. Traditional materials and designs may become impractical: substrate-integrated architectures and integrated-on-chip solutions have been explored but often suffer from low gain or narrow bandwidth. THz antenna prototypes have included on-chip dipoles, slot elements, leaky-wave conFiguretions, and metamaterial-inspired structures. Nonetheless, the microstrip patch remains attractive for integration with electronics as novel techniques such as frequency reconFiguretion, defected ground structures, and hybrid materials have been investigated to boost its performance. In particular, reconFigurebility and miniaturization are of great interest; solutions include tunable metasurfaces, integrated MEMS or liquid-metal elements, and exotic substrates. Yet many of these approaches still rely on bulk metals or dielectrics, which incur high ohmic and dielectric loss at THz [4–7].

Despite these advantages, graphene also has notable limitations. A monolayer of graphene, while an excellent conductor per atomic thickness, has a relatively low sheet conductivity compared to metal layers of comparable thickness. In the microwave band, graphene (even when doped to moderate Fermi levels) is orders of magnitude more resistive than copper; consequently pure-graphene antennas at sub-THz or lower frequencies tend to exhibit poor efficiency. Even at THz frequencies graphene's losses, arising from finite mobility and scattering, can severely degrade performance unless it is biased, stacked, or integrated into hybrid structures. Recent device demonstrations that use stacked graphene and hexagonal boron nitride show modest gains but also reveal the practical difficulty of producing high-efficiency graphene radiators. These limitations have motivated exploration of alternative two-dimensional carbon allotropes that might combine graphene-like plasmonic behavior with improved intrinsic conductivity or an energy gap that aids impedance matching [2, 8–10].

Among emerging 2D carbon materials, graphynes form a family of predicted allotropes obtained by inserting acetylenic linkages into the graphene lattice. The class includes graphyne, graphdiyne and higher members characterized by one, two, or more consecutive acetylenic bonds between hexagonal rings. The structural diversity of graphynes leads to a variety of predicted electronic properties; notably, several graphyne polymorphs are predicted to possess intrinsic bandgaps in contrast to graphene's gapless spectrum. The presence of a bandgap can be advantageous

for antenna applications by shifting plasmonic response and enabling bias-free switching, while high predicted carrier mobilities promise lower loss than conventional disordered films. Theoretical studies also indicate Dirac-cone-like features and anisotropic transport in selected graphyne structures. In particular, γ-graphyne, a specific topology in the graphyne family, has been predicted to exhibit a direct bandgap and favorable electronic properties that may support plasmonic-like response in the THz region[11–14].

Synthesis of high-quality, large-area γ-graphyne remains a major experimental challenge. To date, reported samples are generally limited to small domains or to materials with a significant density of defects; large-scale, high-quality γ-graphyne films with reproducible electronic properties have not yet been widely realized. Consequently, most insight into γ-graphyne's optical and transport behavior originates from first-principles calculations. Density functional theory (DFT) studies predict electronic band structures, phonon stability, and optical responses, while quantum transport calculations and Kubo-type formalisms are used to estimate frequency-dependent conductivities. These atomistic predictions provide crucial input parameters for electromagnetic device-level modeling when experimental material data are unavailable [13, 15, 16].

In this paper, we present design and analysis of microstrip patch antennas operating in the THz band whose radiating element is formed by γ-graphyne. To capture the material's intrinsic electromagnetic response we compute γ-graphyne's frequency-dependent complex conductivity from first principles. Our methodology combines DFT electronic structure calculations with the Kubo–Greenwood formalism to obtain the complex surface conductivity $\sigma(\omega)$, including interband and intraband contributions and a discussion of scattering and broadening. We then incorporate $\sigma(\omega)$ into full-wave finite-element electromagnetic simulations of microstrip patches on realistic dielectric substrates, modeling the 2D material either as a surface conductivity boundary or as an ultrathin volumetric layer depending on the simulation framework. This first-principles informed multiscale approach bridges atomistic theory and antenna engineering and ensures that the simulated antenna response reflects the material's predicted dispersive behavior[15, 17, 18].

Our results show that γ-graphyne patches can resonate in the sub-THz band with significant miniaturization compared to metallic counterparts while exhibiting radiation patterns and directivities suitable for link-level applications. The presence of an intrinsic bandgap in γ-graphyne modifies the plasmonic dispersion relative to graphene and shifts the plasma frequency, enabling distinct bandwidth and tunability characteristics without requiring large bias voltages. Compared to graphene-based patches of identical geometry and realistic doping, γ-graphyne exhibits different efficiency and bandwidth trends arising from its unique $\sigma(\omega)$. We also analyze sensitivity to substrate permittivity and material scattering rates, and discuss fabrication and measurement feasibility with current thin-film techniques. By combining first-principles materials modeling with device-scale EM simulation, we demonstrate a new material-driven route to compact THz radiators that may complement existing graphene and metal-based designs [18–20].

In summary, the introduction has reviewed key aspects of THz antennas, material-driven limitations of conventional metals and graphene, and the emerging promise of 2D carbon allotropes such as γ-graphyne. We emphasize a methodology that couples DFT/Kubo calculations with full-wave EM simulation to produce realistic antenna predictions when experimental material data are lacking.

The following sections present computational details, the extraction of *σ(ω)* from first principles, the EM modeling approach, and antenna performance results that assess γ-graphyne's potential as a THz microstrip radiator, where obtaining the Specific Absorption Rate (SAR) is also emphasized.

2. Methodology

The atomic geometry and electronic ground state of γ-graphyne were obtained using density functional theory (DFT) calculations as implemented in SIESTA. Norm-conserving pseudopotentials together with a double-ζ polarized basis set were used to represent valence states; the exchange–correlation functional was treated within the generalized gradient approximation of Perdew, Burke and Ernzerhof (PBE). A vacuum region exceeding 10 Å was introduced normal to the plane to avoid spurious interactions between periodic images. Brillouin zone sampling was performed with a dense Monkhorst–Pack mesh (for example 11×11×1 for the unit cell) and convergence tests on k-point density and basis cutoff were conducted to ensure forces and total energy thresholds were satisfied. The relaxed lattice, band structure and density of states resulting from this procedure were used to determine interband transition thresholds and the electronic occupation required for the subsequent linear-response calculations [18, 21].

The complex dielectric tensor ε(ω) was computed using a Kubo–Greenwood linear-response formalism applied to the DFT eigenvalues and eigenstates. The imaginary part of ε(ω) was obtained from explicit interband transition sums and the real part recovered via Kramers–Kronig relations; this yields the complex dielectric response across the frequency interval of interest for the THz antenna study [19, 22, 23]. The volumetric complex conductivity $\sigma_{\mathrm{vol}}(\omega)$ is related to *ε(ω)* by

$$\sigma_{\mathrm{vol}}(\omega) = -\,\mathrm{i}\,\omega\varepsilon_0[\varepsilon(\omega) - 1] \qquad (1)$$

where ε_0 is the vacuum permittivity and ω the angular frequency. The (1) was evaluated numerically from the computed dielectric function using a controlled broadening parameter to emulate carrier scattering; the dependence of *σ(ω)* on broadening and k-point density was quantified to bound numerical uncertainty [20, 23].

Because γ-graphyne is atomically thin, the volumetric conductivity is converted to an effective surface conductivity $\sigma_s(\omega)$ for use in electromagnetic simulations:

$$\sigma_s(\omega) = \sigma_{\mathrm{vol}}(\omega)\, t_{\mathrm{eff}}, \qquad (2)$$

and implemented on the 2-D patch surface in COMSOL. This boundary representation has been validated against equivalent thin-volume implementations and is standard practice for graphene-family antenna modeling [24, 25].

Initial patch dimensions were estimated with classical microstrip relations adapted to the effective permittivity of the substrate and to thin-film effects. The approximate expression for the patch width W_p used to initialize the design is

$$W_p = \frac{c}{2f_r}\sqrt{\frac{2}{\varepsilon_s + 1}}, \qquad (3)$$

where c is the speed of light in vacuum, f_r is the target resonant frequency and ε_r is the substrate permittivity [4]. The effective dielectric constant ε_{eff} that accounts for fringing is approximated by:

$$\varepsilon_{\text{eff}} = \frac{\varepsilon_s + 1}{2} + \frac{\varepsilon_s - 1}{2}\left[\sqrt{1 + 12\frac{h}{W_p}}\right], \qquad (4)$$

with h denoting substrate thickness. The normalized length extension ΔL/h due to fringing fields is estimated with the empirical formula:

$$\frac{\Delta L}{h} = 0.412\frac{\left(\varepsilon_{eff} + 0.3\right)\left(\frac{W_p}{h} + 0.264\right)}{\left(\varepsilon_{eff} - 0.258\right)\left(\frac{W_p}{h} + 0.8\right)} \qquad (5)$$

and the corrected resonant patch length is then

$$L_p = \frac{c}{2f_r\sqrt{\varepsilon_s}} \qquad (6)$$

These closed-form relations were implemented in GNU Octave to provide initial geometry values before full-wave optimization [4, 18, 26]. Full-wave simulations were carried out in COMSOL Multiphysics using the Electromagnetic Waves, Frequency Domain physics interface. The γ-graphyne patch was modelled as a 2-D impedance boundary with $\sigma_s(\omega)$ imported as a complex, frequency-dependent parameter. Wave ports excite the inset microstrip feed and provide the voltage/current necessary to compute the input impedance Z_{in}. Perfectly matched layers surround the computational domain; meshes were refined to ensure at least ten elements per wavelength in the dielectric and local refinement around edges and holes was used for GPBG variants[27].

The reflection coefficient (S_{11}) is computed from the simulated input impedance Z_{in} and the reference impedance Z_0 = 50 Ω:

$$S_{11}(\omega) = \frac{Z_{\mathrm{in}}(\omega) - Z_0}{Z_{\mathrm{in}}(\omega) + Z_0}. \qquad (7)$$

Radiated power P_{rad} is obtained by far-field integration of the Poynting vector; dissipated (ohmic) power P_{loss} is obtained by integrating the resistive power density over the conductive sheet. Radiation efficiency η is defined as

$$\eta(\omega) = \frac{P_{\mathrm{rad}}(\omega)}{P_{\mathrm{rad}}(\omega) + P_{\mathrm{loss}}(\omega)}. \qquad (8)$$

All S-parameters, input impedance, VSWR, far-field patterns, gain and current distributions presented in the Results were extracted according to these procedures [25, 28].

To bound numerical uncertainty we performed DFT convergence studies (basis size, k-point mesh, broadening) and electromagnetic sensitivity tests (mesh refinement, PML thickness and port definition). We quantified the influence of the broadening parameter on $\sigma_s(\omega)$ and the sensitivity of resonance frequency and S_{11} to mesh and FE tolerances; these checks follow best practice for multi-scale modelling and mirror procedures used in earlier graphene-THz antenna studies [4, 29, 30]. Tabulated $\sigma_s(\omega)$ data and key simulation inputs were prepared for reproducibility.

3. Results and discussion

This section examines the electromagnetic consequences of the first-principles material response for γ-graphyne and quantifies the antenna performance for the four topology variants studied: GN (plain patch), GPBG (photonic band-gap substrate), GNano (edge nanoribbons), and GNano+PBG (hybrid). We (i) interpret the DFT+Kubo outputs in terms of guided-mode physics, (ii) link microscopic material properties to antenna observables through explicit relations, (iii) describe Figures 2 and 3 in detail, and (iv) analyze S_{11}, input impedance, VSWR, radiation efficiency, gain and current distributions. Numerical spectra and geometry values quoted below are those obtained from the COMSOL simulations using the $\sigma_s(\omega)$ tables exported from the DFT/Kubo calculations.

3.1 Mapping material response to guided-mode and antenna behaviour.

The Fig. 1 presents the DFT+Kubo derived optical quantities: the real and imaginary parts of the permittivity *ε(ω)* and permeability *μ(ω),* and the effective surface conductivity $\sigma_s(\omega)$ used as the surface boundary in COMSOL. The conductivity exhibits a pronounced low-THz intraband-like maximum and a finite imaginary component across the design band; representative numerical values taken from the exported tables include *ε_1(0.1 THz) ≈ 10.86 and σ_1(0.4 THz) ≈ 2.66 nS*. These spectral tables were directly imported into the electromagnetic model.

The following relations connect material quantities to guided-mode and antenna observables. The guided wavelength λ_g is set by the modal propagation constant $\beta(\omega)$:

$$\lambda_g(\omega) = \frac{2\pi}{\beta(\omega)}. \qquad (9)$$

A first-order Fabry–Pérot standing-wave criterion for the fundamental patch resonance relates the effective electrical length L_{eff} to the guided half-wavelength:

$$L_{\text{eff}} = \frac{\lambda_g(\omega_r)}{2}. \qquad (10)$$

consequently, a design estimate for the resonant frequency is

$$f_r \approx \frac{c}{2L_{\text{eff}}\sqrt{\varepsilon_{\text{eff,g}}(\omega_r)}}, \qquad (11)$$

where $\varepsilon_{\text{eff,g}}(\omega)$ denotes the effective dielectric loading experienced by the guided mode (this differs from the quasi-static ε_eff used for conventional metallic microstrip patches because field confinement is governed by σ_s). These relations explain why an increase in the real part of $\sigma_s(\omega)$ (stronger conduction) typically shortens λ_g and enables physical miniaturization of the patch for a fixed resonant frequency. Power dissipated in the conductive sheet is computed from the surface resistivity and the simulated surface current density J(r). Defining the surface resistivity R_s = Re[$1/\sigma_s(\omega)$], the dissipated (ohmic) power is

$$P_{\text{loss}}(\omega) = \frac{1}{2}\int_S R_s(\omega) \; |\, \mathbf{J}(\mathbf{r},\omega) \,|^2 \; \mathrm{d}S. \qquad (12)$$

P_{rad} is computed by far-field integration of the Poynting vector; defining a reference modal current amplitude I_0, the radiation and loss contributions can be cast as equivalent resistances

$$R_{\text{rad}}(\omega) = \frac{2P_{\text{rad}}(\omega)}{|\, I_0 \,|^2}, \qquad (13)$$

$$R_{\text{loss}}(\omega) = \frac{2P_{\text{loss}}(\omega)}{|\, I_0 \,|^2}. \qquad (14)$$

Thus the input impedance decomposes into radiative, dissipative and reactive parts:

$$Z_{\mathrm{in}}(\omega) = R_{\mathrm{rad}}(\omega) + R_{\mathrm{loss}}(\omega) + \mathrm{i}X(\omega). \qquad (15)$$

The radiation efficiency follows directly as the ratio between radiative and accepted power:

$$\eta(\omega) = \frac{R_{\mathrm{rad}}(\omega)}{R_{\mathrm{rad}}(\omega) + R_{\mathrm{loss}}(\omega)}. \qquad (16)$$

The (9)–(16) emphasize two central design tensions. First, raising the real part of $\sigma_s(\omega)$ increases β (shortens λ_g) and therefore enhances miniaturization potential, but confinement also amplifies local $|J|^2$ in regions where R_s may be non-negligible, which increases R_{loss} and can degrade η. Second, substrate engineering (for example a PBG lattice) can reduce substrate-guided modes and thereby reduce P_{loss} for a fixed modal current distribution, effectively increasing $R_{\mathrm{rad}}/R_{\mathrm{loss}}$ and improving η even when $\sigma_s(\omega)$ retains some imaginary component. These phenomena have been widely discussed in graphene-patch literature and are consistent with classical PBG patch studies [31–33][34, 35].

Fig. 1(a–c) displays the computed $\varepsilon(\omega)$, $\mu(\omega)$ and $\sigma_s(\omega)$ curves used as the electromagnetic input. Key observations and implications:

• Permittivity and permeability loading. The computed ε(ω), μ(ω) increase the electromagnetic loading of the guided mode (higher $\varepsilon_{\mathrm{eff,g}}$ in (12)), which influences both miniaturization and matching. Numerical entries from the material tables are used directly to compute $\varepsilon_{\mathrm{eff,g}}$ during COMSOL modal solves and thereby determine resonance shifts when geometry or substrate are modified.

• Conductivity spectral shape. The real part $\sigma_1(\omega)$ shows a pronounced peak in the low THz range. This peak defines a frequency window where guided-mode confinement is strongest and where a γ-graphyne patch can be electrically much smaller than a metallic patch designed for the same free-space wavelength. The COMSOL models import the full $\sigma_s(\omega)$ table so that both the dispersive shortening of λ_g and the frequency-dependent losses are captured in the simulated S-parameters and far fields

• Imaginary conductivity and loss. The imaginary part $\sigma_2(\omega)$ is non-zero across the design band and yields a non-negligible $R_s(\omega)$ via (12). Consequently, off-resonance excitation and surface-wave coupling to the substrate increase dissipative loss; this is observed in the simulated efficiency curves and motivates the use of PBG substrate variants to suppress trapped surface modes.

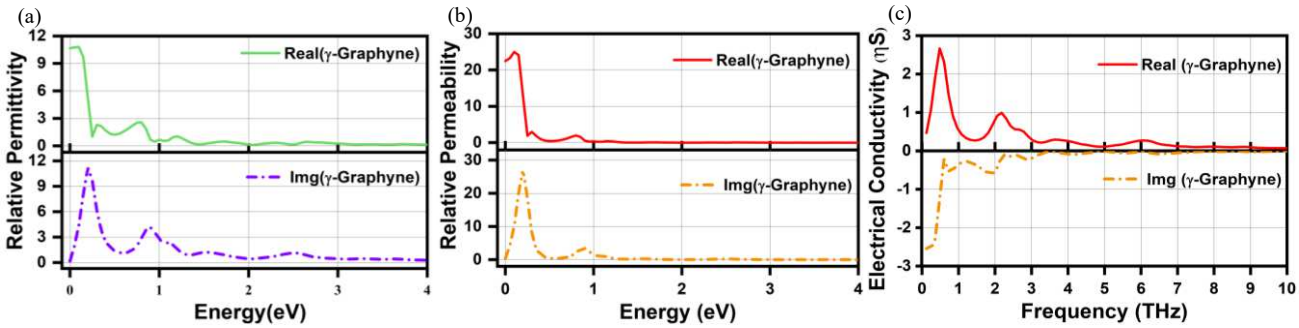


Figure 1. Real and imaginary, respectively: **(a)** $\varepsilon_1(\omega)$ and $\varepsilon_2(\omega)$; **(b)** $\mu_1(\omega)$ *and* $\mu_2(\omega)$; **(c)** $\sigma_1(\omega)$ *and* $\sigma_2(\omega)$.

3.2 Quantitative electromagnetic results and interpretation

Fig. 2(a) presents the reference antenna (GN antenna), shown in both two-dimensional (2D) planar view and three-dimensional (3D) rendering. Fig. 2(b) depicts the crystal lattice of y-graphyne, along with the simplified unit cell adopted in this study, which was reduced to 12 carbon atoms (highlighted in light blue), while preserving the essential structural characteristics of the material.

Fig. 2(c–f) illustrate the different configurations of the y-graphyne-based antennas analyzed in this work, namely GN, GPBG, GNano, and GNano+PBG. The initial geometric parameters used in the modeling are indicated in the figure caption and were subsequently refined through full-wave electromagnetic optimization. The adopted dimensions are as follows: substrate width $W_s = 40\ \mu m$and length $L_s = 48\ \mu m$; patch width $W_p = 30\ \mu m$and length $L_p = 22\ \mu m$; inset feed width $W_f = 5.5\ \mu m$; substrate relative permittivity $\varepsilon_r = 4.4$; and substrate thickness $h = 3\ \mu m$ ed tuning because R_{in} and X_{in} shift more substantially.

Interpretations tied to the geometry:

• GN (plain patch) — baseline resonator whose resonance and efficiency reflect the raw impact of σ_s (ω) and the chosen patch dimensions obtained via closed-form relations and subsequent tuning.

• GNano (edge nanoribbons) — nanoribbons concentrate edge currents and modify the modal phase distribution, which tends to increase R_{rad} relative to R_{loss} when currents are redistributed to regions favoring radiation (edges). In practice GNano reduces the reactive term X(ω) at resonance and provides deeper S_{11} minima with little change to fabrication complexity relative to full substrate patterning. This behaviour mirrors graphene edge-engineering strategies [32].

• GPBG (PBG substrate) — by choosing the lattice constant a in the PBG to satisfy the Bragg-type criterion near $\lambda_g/2$ (as described in Section 2), the substrate opens a stop band for surface waves and reduces trapped guided energy beneath the patch; this reduces P_{loss} and increases η. The PBG design improves peak radiation performance but modifies $\varepsilon_{\text{eff,g}}$ and therefore shifts f_{c}.

• GNano+PBG (hybrid) — combines the impedance-shaping and edge-radiation benefits of GNano with the substrate loss suppression of GPBG, producing the best peak gain in simulations but requiring fe.

Parameters	$W_s \times L_s$	$W_p \times L_p$	$W_f \times L$	$L_i \times g$
μm^2	40 × 48	30 × 22	5.5 × 8.5	9 × 0.45

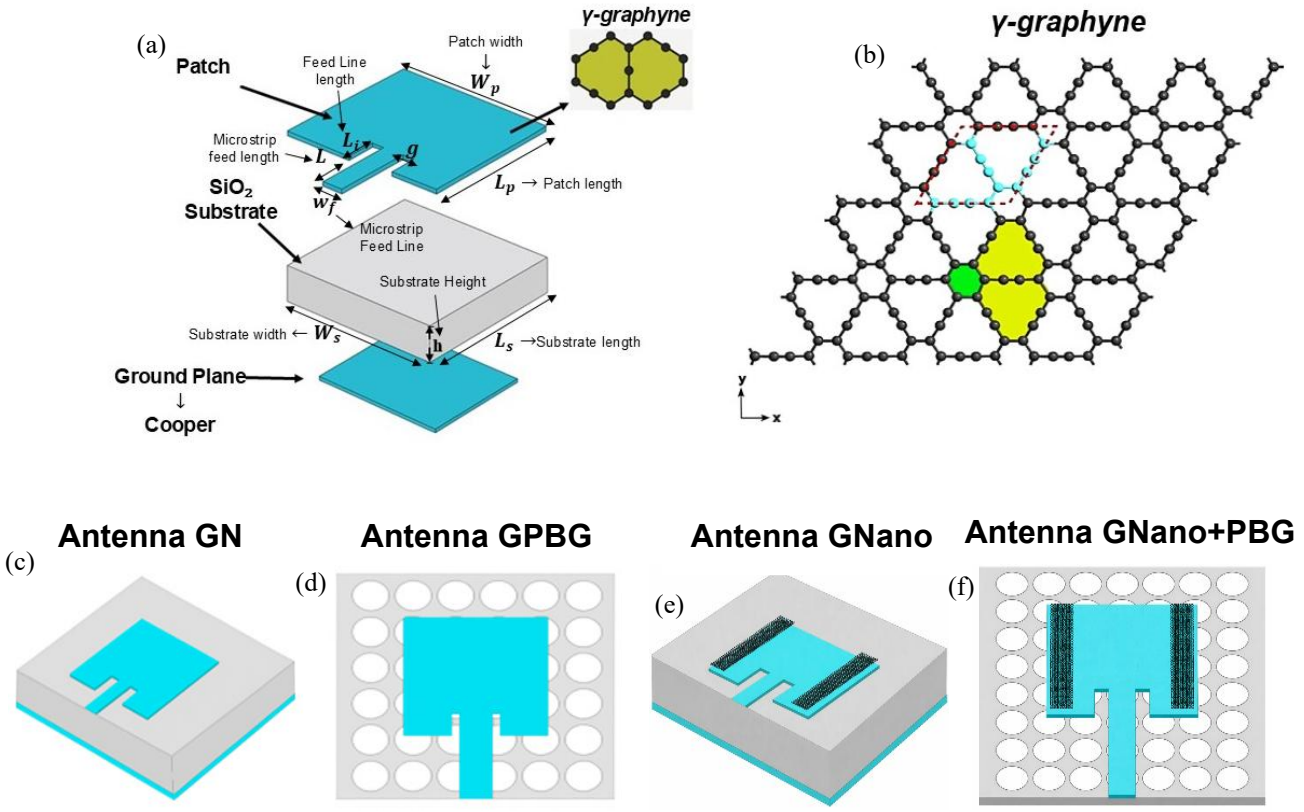


Figure 2. a) 2-D and 3-D design of the *MPA* with γ-graphyne about SiO_2 substrate and cooper ground plane via GNU Octave software. The parameters of the antenna are $f_r = 3.0\ THz$, $h = 3.0\ \mu m$, and $\varepsilon_s = 4.4$ were obtained $W_s = 40.0\mu m$, $L_s = 48.0\mu m$, $W_p = 30.0\ \mu m$, $L_p = 22.0\ \mu m$, $W_f = 5.5\mu m$, $L = 8.5\mu m$, $L_i = 9.0\ \mu m$ and $g = 0.457\ \mu m$. b) Crystal lattice: the atoms highlighted in blue represent the unit cell in a simplified configuration. In dark green, the benzene ring located at the center of the replicated unit cell is observed. The rings with triangular geometry correspond to a more complex unit cell. c) Standard conFiguretion of the γ-Graphyne-based microstrip antenna (*GN antenna*), d) Antenna with periodic structure on the substrate, incorporating photonic crystals (*GPBG antenna*), e) Antenna with γ-Graphyne nanostrips coupled to the patch (*GNano antenna*), and f) Hybrid antenna with periodic structure on the substrate and nanostrips on the patch (*GNano+PBG antenna*).

All antenna performance curves reported here are derived from COMSOL frequency-domain simulations that used the $\sigma_s(\omega)$ tables exported from the DFT+Kubo computations. Key comparative findings S_{11} minima and resonant frequencies. GN and GNano produce the deepest S_{11} minima (≈ −34 dB) near 3.28–3.29 THz; GPBG and GNano+PBG shift the resonance upward by ≈ 0.2–0.3 THz and show shallower S_{11} minima (≈ −22 to −19 dB). The resonance shift reflects the modification of $\varepsilon_{\mathrm{eff,g}}$ and guided dispersion introduced by substrate patterning. Input impedance and VSWR. At resonance GNano yields $R_{\mathrm{in}} \approx 51.16\ \Omega$ and $X_{\mathrm{in}} \approx +1.42\ \Omega$ (VSWR ≈ 1.03), making it the best match to 50 Ω without added matching. GPBG and the hybrid present higher R_{in} and larger reactive terms, indicating that feed or matching network adjustments would be beneficial for those topologies.

Radiation efficiency and gain. GPBG and GNano+PBG achieve slightly higher peak gain and η (peak gains ≈ 6.32–6.37 dB and efficiencies ≈ 82–83% at their respective fc) because the PBG reduces substrate trapping and redirects accepted power into radiation. Off-resonance efficiency decreases sharply where dissipative loss and substrate modes dominate. These trends match the expectations

from via (12)–(16). Current distributions. Current density maps indicate GNano concentrates currents at the patch rim and along the nanoribbons, increasing radiative contribution per unit accepted power; the hybrid shows combined features: edge concentration plus reduced substrate mode leakage. Quantitative maxima of |J| are consistent with the higher $R_{\mathrm{rad}}/R_{\mathrm{loss}}$ ratios observed for PBG variants.

From the relations (9)–(11) and the numerical results, the design trade-space for γ-graphyne microstrip radiators can be summarized as follows:

1. For minimal fabrication complexity and best raw impedance match, GNano is preferred because edge shaping yields R_{in} close to 50 Ω and deep S_{11} minima.
2. To maximize peak gain and radiation efficiency (when fabrication permits substrate patterning), GPBG or GNano+PBG are recommended because suppressing substrate waves reduces P_{loss} and increases η; however, feed redesign or matching networks are likely required to achieve best system performance.
3. Improvements in intrinsic material quality (reduced scattering, higher mobility) directly reduce $R_{\mathrm{s}}(\omega)$ in via (13), lower R_{loss}, and thereby increase η without geometric changes; hence materials synthesis and processing are high-impact levers for improved figures of merit.
4. Sensitivity to fabrication tolerances. Convergence and parametric sweeps in the Methodology show that small geometric deviations (a few percent in patch length or PBG lattice constant) produce measurable shifts in f_{c} of tens to hundreds of GHz in the THz band. This implies that lithographic and etching control strongly affect final performance; designers should plan for tunable matching elements or post-fabrication trimming in experimental validation campaigns.
5. Temperature and environmental influences. Changes in carrier scattering with temperature modify $\sigma_s(\omega)$; since η depends critically on R_{s} via (12), reducing scattering (for example by lower temperature or improved synthesis) yields marked efficiency gains without geometry changes. This coupling emphasizes the joint importance of materials engineering alongside electromagnetic design.
6. PBG trade-offs and manufacturability. While PBG patterning reduces substrate trapping, it can also perturb feed coupling and scatter edge currents. The hybrid GNano+PBG produces higher peak gains in simulation but demands optimized feed and perhaps graded or partial PBG implementations to balance performance gains with fabrication complexity. Classical PBG literature suggests that judiciously designed partial PBG lattices can recover much of the benefit while easing manufacturing.
7. Application-driven choices. For compact on-chip THz links and short-range emitters where footprint matters more than absolute peak efficiency, GN or GNano are attractive. For free-space transmitters or sensing front-ends where link budget is critical, GPBG or GNano+PBG combined with low-loss substrates or active tuning elements will be more appropriate.

The interplay between guided confinement, dissipation and PBG-mediated surface-wave suppression aligns with established findings in graphene and PBG patch literatures [32-36]. PBG substrates have long been used to reduce surface-wave trapping and improve patch efficiency [31],

while graphene-based patch work demonstrates tunable Fabry–Pérot resonances and significant miniaturization in the THz band, with caveats regarding spatial dispersion and loss [32], [35]. Our γ-graphyne results adopt these lessons and quantify the numerical differences arising from γ-graphyne's computed $\sigma_s(\omega)$.

The electromagnetic behavior of γ-graphyne patches is strongly shaped by two concurrent design elements: the introduction of narrow γ-graphyne nanoribbons at the patch perimeter and the use of a photonic bandgap (PBG) substrate to suppress substrate-guided modes. Nanoribbons carved from extended γ-graphyne sheets inherit the one-dimensional quantum confinement and edge-dependent electronic structure documented in first-principles studies. Zigzag and armchair γ-graphyne nanoribbons present width-dependent band gaps and distinct edge states, so that narrower zigzag ribbons can concentrate low-loss, edge-localized carriers and produce a more metallic local response than wider ribbons; this electronic trend underpins the choice of narrow zigzag nanoribbons as current-concentrating features on the patch edge. The tunability of nanoribbon electronic structure with ribbon width and edge morphology therefore provides a materials lever to control the surface conductivity $\sigma_s(\omega)$ locally at the patch rim and to redistribute modal currents towards regions that radiate more efficiently [36, 37].

From an electromagnetic standpoint, placing nanoribbons at the non-radiating edges acts as an impedance-shaping geometry that modifies the local modal phase and amplitude near the patch rim. When edge currents are enhanced and shifted into regions of higher radiation aperture, the effective radiation resistanceR_{rad} increases relative to the dissipative resistance R_{loss} associated with finite sheet conductivity. This redistribution reduces the reactive loading at the input and deepens the S_{11} minima without necessarily increasing the physical patch footprint. The effect is particularly noticeable for atomically thin conductors whose dispersive surface conductivity yields strong confinement of guided modes; by concentrating currents at the edge, the nanoribbons trade increased local current density for improved radiation efficiency because the radiated power scales favorably with edge current in microstrip patch geometries. The numerical models reported in this work explicitly use the DFT+Kubo derived $\sigma_s(\omega)$ tables so that these redistribution effects are captured with material realism [36, 37].

The PBG substrate provides a complementary, substrate-side mechanism for improving radiation performance. A two-dimensional periodic array of air inclusions or dielectric columns opens stop bands for surface waves when the lattice period a satisfies the Bragg-type condition for the guided mode. Expressed in terms of the guided propagation constant β(ω), the Bragg (stop-band) criterion reads

$$\beta(\omega)\, a \approx \pi \Rightarrow a \approx \frac{\pi}{\beta(\omega)} = \frac{\lambda_g(\omega)}{2}, \qquad (17)$$

where the guided wavelength $\lambda_g$is $\lambda_g = 2\pi/\beta$and β is related to the modal effective permittivity by $\beta \approx k_0\sqrt{\varepsilon_{\mathrm{eff},g}(\omega)}$with $k_0 = \omega/c$. Choosing a within the approximate half-guided-wavelength condition places the operating band inside the PBG stop band for substrate guided modes and strongly suppresses trapped energy beneath the patch. The uniplanar compact PBG (UC-PBG) family and related photonic crystal substrates implement this concept while remaining fully compatible with planar fabrication processes, and they have been shown to increase broadside gain and reduce surface-wave loss when placed around or beneath a patch [38].

A compact and robust way to quantify the trade between radiation and dissipation uses surface resistivity and modal currents. For an atomically thin conductor described by surface conductivity σ_s (ω), define the surface resistivity

$$R_s(\omega) = \mathrm{Re}\,\{1/\sigma_s(\omega)\}. \qquad (18)$$

The ohmic (dissipated) power can be written as

$$P_{\mathrm{loss}}(\omega) = \frac{1}{2}\int_S |\, J(r,\omega)\,|^2 \;\; R_s(\omega)\, dS, \qquad (19)$$

while the radiated power P_{rad} is obtained from the far-field Poynting integral. Radiation and loss contributions may be cast as equivalent resistances referred to a modal current amplitude I_0, so that

$$Z_{\mathrm{in}}(\omega) = R_{\mathrm{rad}}(\omega) + R_{\mathrm{loss}}(\omega) + jX(\omega), \eta(\omega). \qquad (20)$$

These compact expressions clarify the two main levers for performance improvement: increase R_{rad} by reshaping currents (for example with edge nanoribbons), or reduce R_{loss} by suppressing substrate guided energy (for example with a PBG substrate). In practice the best results come from a mixed strategy because the nanoribbons increase edge radiation while the PBG lattice reduces trapped substrate energy; the combination yields larger $R_{\mathrm{rad}}/R_{\mathrm{loss}}$ and higher peak gain, albeit at the cost of feed tuning because both $\varepsilon_{\mathrm{eff},g}$ and β are altered by the PBG lattice [38, 39].

Design and fabrication implications follow directly. Nanoribbon width and termination must be selected to balance metallic-like behavior with manufacturability; the literature reports that zigzag γ-graphyne ribbons often show the stronger edge conduction needed for these applications but require careful width control to avoid unwanted gap opening [36, 37]. The PBG lattice constant a and filling ratio should be tuned to the guided dispersion of the γ-graphyne-loaded mode rather than to the free-space wavelength because field confinement in atomically thin conductors shifts β substantially. Finally, because both nanoribbons and PBG lattices increase sensitivity of fc to small geometric variations, practical implementations should plan for modest post-fabrication matching or tunability. Recent THz implementations confirm that PBG-based substrates can be synthesized and optimized to raise gain and efficiency in the THz band, supporting the hybrid approach adopted here [39].

3.3. Microstrip Antenna Analysis: Performance Evaluation

Fig. 3(a-b) presents the behavior of the complex input impedance Z_{in}. The real component R_{in} and the imaginary component X_{in} of the Z_{in} are key parameters for characterizing antenna performance and impedance matching. In fig. 3(a), the R_{in} for the *GN* and *GNano* antennas, a main peak is observed around *2.4 THz*, with approximate values of *555 Ω* and *560 Ω*, respectively, along with a secondary maximum at *3.44 THz*, with resistances of about *155 Ω* (*GN*) and *149 Ω* (*GNano*). For the *GPBG* and *GNano+PBG* antennas, the main R_{in}peaks occur at *2.71 THz* and *2.74 THz*, with magnitudes close to *561 Ω* and *566 Ω*, respectively, accompanied by secondary maxima at *3.67 THz ≈141 Ω* and *3.73 THz ≈127 Ω*. Fig. 3(b) The imaginary part X_{in}, where four sets of characteristic peaks are identified. For the *GN* and *GNano* antennas, main positive peaks appear around *2.43 THz*, with approximate values of *292 Ω* and *294 Ω*, in addition to secondary maxima at *3.51 THz ≈119 Ω* and *3.51 THz ≈ 115 Ω*, respectively. Near the resonance frequency, a sign change in X_{in} is observed, with values close to *−1.79 Ω* at *3.28 THz* and *1.42 Ω at 3.29 THz*, indicating the transition between inductive and capacitive regimes. For the *GPBG* and *GNano+PBG* conFiguretions, the main positive X_{in} peaks are located at *2.83 THz ≈259 Ω* and *2.86 THz≈263 Ω*. In contrast, the dominant negative peaks appear at 2.43 *THz* for GN and GNano, with magnitudes near *−292 Ω* and *−294 Ω*, while for the *GPBG* and *GNano+PBG* antennas these minima occur at *2.59 THz ≈−294 Ω* and *2.61 THz ≈ −261 Ω*. In general, it is observed that both R_{in} and X_{in} exhibit approximately symmetric behavior around the f_c of each antenna, a typical characteristic of well tuned resonant structures.

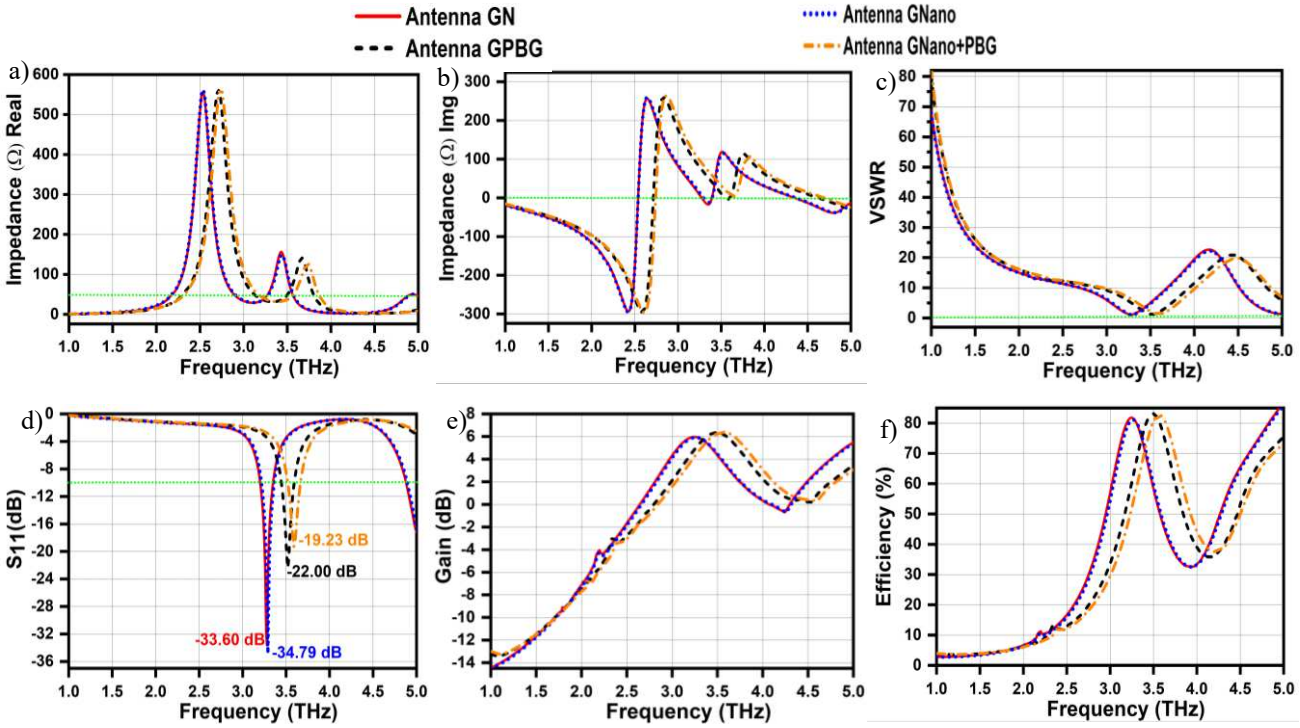


Figure 3. (a) S_{11} , **(b)** Z_{in} and (c) *VSWR* for the microstrips antennas design with f_r = *3 THz*, h = *3 μm*, ε_s = *4.4*, W_s = *40μm*, L_s = *48μm*, W_p = *30 μm*, L_p = *22 μm*, W_f = *5.5μm*, L = *8.5μm*, L_i = *9 μm* and g = *0.457 μm*. **(d)** S_{11}, **(e)** *Gain* (*G*) and **(f)** *Radiation Efficiency* (*%*) as function of the *THz* band (1.0-5.0 *THz*) for microstrip antennas with *y-graphyne* patch via COMSOL software.

At its resonance frequency, $f_c = 3.29\ THz$, the complex impedance assumes the approximate value of $Z_{in} = (51.16 + j1.42)\ \Omega$. For comparison, the values obtained at the respective resonance frequencies are: $Z_{in} = (51.10 - j1.79)\ \Omega$ for the *GN* antenna, $Z_{in} = (55.19 + j6.12)\ \Omega$ for the *GPBG* antenna, and $Z_{in} = (55.46 + j10.12)\ \Omega$ for the *GNano+PBG* antenna. It is observed that the R_{in} values for the *GNano* and *GN* antennas are very close to the ideal *50 Ω*, being *51.16 Ω* and *51.10 Ω*, respectively. However, the reactive component of *GNano* ($X_{in} = 1.42\ \Omega$) is closer to zero compared to that of *GN* ($X_{in} = -1.79\ \Omega$), indicating better impedance matching at the resonance frequency. Therefore, the R_{in} and X_{in} values of the *GNano* antenna are closest to the ideal targets of 50 Ω and 0 Ω, evidencing its superior performance

Fig. 3(c) presents the behavior of the *Voltage Standing Wave Ratio* (*VSWR*), This parameter is directly associated with the reflection coefficient S_{11} and is widely used to evaluate the quality of impedance matching between the feed line and the antenna. Under ideal matching conditions, *VSWR* reaches a minimum value of 1.0, indicating no reflected power back to the source [40]. The obtained results demonstrate satisfactory performance for all analyzed configuretions. Specifically, the *VSWR* values are *1.04*, *1.03*, *1.16*, and *1.24* at the frequencies of *3.28 THz*, *3.29 THz*, *3.52 THz*, and *3.59 THz*, corresponding to the *GN*, *GNano*, *GPBG*, and *GNano+PBG* antennas, respectively. These values, close to unity, confirm the good impedance matching of the proposed antennas within the consider ed operating band.

Fig. 3 (d) illustrates the behavior of the reflection coefficient S_{11} in the *1–5 THz* range, showing several resonance peaks associated with the f_c. The green dashed line indicates the widely adopted *−10 dB* criterion for bandwidth definition. The *GN* and *GNano* antennas exhibit nearly identical bandwidths of *BW = 0.14 THz*. For the *GN* antenna, the frequency limits are $f_1 = 3.21\ THz$ and $f_2 = 3.35\ THz$, while for the *GNano* these values are $f_1 = 3.22\ THz$ and $f_2 = 3.36\ THz$. Consequently, their fractional bandwidths B_p are *4.26%* and *4.25%,* respectively. Furthermore, the minimum S_{11} values indicate excellent impedance matching for both conFiguretions, with *−33.65 dB* for the *GN* antenna and *−34.79 dB* for the *GNano*, confirming that both operate stably and efficiently within the considered frequency band. The *GPBG* and GNano+PBG antennas exhibited S_{11} minima of *−22.00 dB* and *−19.23 dB*, respectively. For the GPBG conFiguretion, the frequency limits defined by the *−10 dB* criterion are $f_1 = 3.45\ THz$ and $f_2 = 3.59\ THz$, resulting in B_p of *3.97%*. The *GNano+PBG* antenna operates between $f_1 = 3.53\ THz$ and $f_2 = 3.66\ THz$, with $B_p = 3.62\%$.

Fig. 3(e-f) present the one-dimensional gain (*in dB*) and the radiation efficiency (*in %*) of the y-graphyne antenna based THz MPAs, operating in the *1.0* to *5.0 THz* range. The maximum gain values observed at their respective f_c were *5.94 dB*, *6.32 dB*, *5.90 dB*, and *6.37 dB* for the *GN*, *GPBG*, *GNano*, and *GNano+PBG* antennas, respectively. Conversely, the gain minima occurred at *4.26 THz*, with values of *−0.61 dB* and *−0.71 dB* for the *GN* and *GNano* antennas, while the *GPBG* and *GNano+PBG* antennas exhibited troughs of *0.37 dB* at *4.54 THz* and *0.32 dB* at 4.59 THz, as illustrated in Figura 3(e). Regarding radiation efficiency, the maximum values reached *81.82%* at *3.25 THz*, *83.07%* at *3.48 THz, 80.73%* at *3.29 THz*, and *82.72%* at *3.56 THz* for the *GN, GPBG, GNano, and GNano+PBG* antennas, respectively. In contrast, the lowest efficiency values were observed at *3.90 THz*, *4.17 THz*, *3.93 THz*, and *4.21 THz*, corresponding to *32.61%, 35.89%, 32.54%,* and *37.70%,* as presented in Fig. 3(f). Radiation efficiency does not reach 100% due to ohmic losses in the conductive material, losses

(a)

associated with the dielectric substrate, and the excitation of surface waves, particularly in very thin or excessively thick substrates.

These limitations are more evident in structures with narrow bandwidths operating at frequencies equal to or greater than 1 GHz (microwave range). Furthermore, such conFiguretions are not suitable for extremely high power levels, as they are subject to dielectric breakdown phenomena unless materials such as air or foam are employed as the substrate [40].

3.3.1 3D confirmatoy results 3D

The radiation pattern of an antenna describes the spatial distribution of radiated electromagnetic power, evaluated in the far-field region where the wave can be approximated as planar. This pattern expresses the angular dependence of the electromagnetic field and is characterized by the vector.The Fig. 4(a–b) presents the 3D radiation patterns, corresponding to the gain, as well as the current density distribution evaluated at their respective f_c.. Fig. 5(a) presents the gain intensities maximum values are: 5.94 dB for the GN antenna: *5.94 dB* for the *GN* antenna, *6.33 dB* for *GPBG*, *5.90 dB* for *GNano*, and *6.38 dB* for *GNano+PBG*. It is observed that the *GNano+PBG* conFiguretion exhibits the highest gain among the evaluated structures, indicating better radiative performance.

Fig. 4(b) illustrates the surface current density of the antennas at their respective f_c. A higher concentration of current (red regions) is noted on the radiating area, especially at the edges of the GNano+PBG antenna, reaching a maximum value of 4.86×10^8 A/m^2, which is superior to the other analyzed conFiguretions. Conversely, the current density shows reduced values, in the range of 0.0 to 1.0×10^8 A/m^2, in the central region and outside the contact area, due to limited current flow in these zones (indicated in blue). Near the feed line and in the transition zones between low and high intensity regions (between blue and red), an intermediate current density is observed, varying approximately between 1.0×10^8 and 4.0×10^8 A/m^2.

The gain (Fig. 3(e)) and efficiency (Fig. 3(f)) plots consistently illustrate the analysis related to co-polarization and cross-polarization, as they exhibit analogous behavior to the evaluation of radiated fields in the main radiation direction and the opposite sense, respectively, whicj helps in confirming the results of Fig. 4(a). For comparison and validation of the obtained results, the works presented in [41, 42].

Furthermore, the use of high-gain antennas becomes essential to enable extremely high transmission rates and superior signal quality levels in future sixth-generation (6G) wireless communication systems operating in the THz band. The THz spectrum (0.1–10 THz) stands out as one of the most promising bands for 6G applications, as it provides very wide bandwidths, potentially reaching up to 100 GHz, and transmission capacities on the order of 1 Tbps. However, the development of high-gain antenna arrays for THz still represents a significant challenge, primarily due to the micrometric dimensions of radiating elements and the limited availability of suitable dielectric materials [43]. In this context, this work focuses on a detailed evaluation of different THz antenna patch architectures and geometries, aiming to optimize radiation properties and gain, thereby helping to mitigate the effects of atmospheric losses that become more pronounced at high frequencies.

The obtained values for the main parameters of the y-graphyne patch microstrip antennas, including VSWR, impedance (Ω), gain (dB), and surface current density (A/m²), are consolidated in Table 1. Meanwhile, the parameters central frequency (f_c, in THz), bandwidth (BW, in THz), reflection coefficient (S_{11}, in dB), gain (dB), and radiation efficiency (%) are presented in Table 2. These results enable an objective comparative analysis, serving as a reference criterion for selecting the most suitable patch type for the microstrip antenna, based on the observed performance of the investigated parameters

Table 1- *VSWR, Impedance* (R_{in} and X_{in}), *Gain* (dB) and *Current Density* for the microstrip antenna with *y-graphyne* patch at f_c and $BW = 0.14$ *THz.*

Parameters	***VSWR***	***R_{in} (Ω)***	***X_{in} (Ω)***	***Ganho (dB)***	***Densidade de corrente (A/m^2)***
Antenna GN	1.04	51.10	-1.79	5.94	$4.00x10^8$
Antenna GPBG	1.16	55.19	6.12	6.93	$4.30x10^8$
Antenna GNano	1.03	51.16	1.42	5.90	$4.41x10^8$
Antenna GNano+PBG	1.24	59.61	10.19	6.38	$4.46x10^8$

Table 2- *f_c (THz), BW (THz), S_{11} (dB)*, *Gain (dB)* and *Efficiency (%)* for the microstrip antenna with *SiO_2* substrate*, COP* plane ground, and *y-graphyne* patch on *THz* range. Comparation with other works using *GRA MPA* and *SiO_2* substrate.

Parameters	***f_c (THz)***	***S_{11} (dB)***	***Eficiência (%)***
Antenna GN	*3.28*	-33.60	81.23
Antenna GPBG	*3.52*	-22.00	82.81
Antenna GNano	*3.29*	-34.79	80.73
Antenna GNano+PBG	3.59	-19.23	82.46

In Ref. [44], *GRA MPA* exhibited: $f_c = 14.97$ *GHz* and *15.0 GHz*, $BW = 1.23$ *GHz* and *1.3 GHz*, $S_{11} = -39.05$ *dB* and *-25.03 dB*, $G = 3.51$ *GHz* and *3.86 GHz*, and $e_o = 82.05$ *%* and *88.12%* (simulated and measured without gate electrode) and $f_c = 15.9$ *GHz* and *16.7 GHz*, $BW = 1.23$ *GHz* and *5.8 GHz*, $S_{11} = -38.18$ *dB* and *-44.7 dB*, $G = 3.54$ *GHz* and *3.97 GHz*, and $e_o = 79.8$ *%* and *88.12%*.

Tripathi and Kumar [45] demonstrated that GRA exhibits superior performance compared to COP for developing antennas operating in the THz band, as COP presents mechanical and structural limitations, making it unsuitable for applications in this frequency range. In [46], a conventional rectangular microstrip patch antenna (RMPA) with micrometric dimensions and a central frequency in the THz region was employed. For $f_c = 0.685$ *THz*, the results obtained were $S_{11} = -30.552$ *dB*, a bandwidth of *26 GHz*, *VSWR = 1.061*, and a gain of *5.145 dB*.

The THz antenna based on γ-graphyne proposed in this work was compared with other high-frequency graphene-based antennas, as presented in Table 3. It is observed that the GBPG antenna exhibits higher gain compared to the model reported in[47]. Furthermore, γ-graphyne-based antennas demonstrate a broader operating bandwidth when compared to the others. These results indicate that the proposed structure achieves consistent performance in the high-frequency range, operating from *3.28 THz* to *3.59 THz* [48–50].

Table 3- Comparative analysis of the proposed THz antenna with recente studies.

Work	f_c	Band Width(THZ)	Gain (dB)
George et al[48]	0.29	0.00149	1.03
Anand et al[49]	0.75	0.05	5.09
Jeyakumar et al[50]	0.3	0.0149	2.19
Bala et al[47]	2.70	0.09	6.59
Antenna GPBG	3.52	0.14	6.93

The obtained results indicate that the proposed structure is well-suited for THz on-chip and short-range systems, where factors such as footprint, integration capability, and compatibility with planar fabrication processes are critical. In emerging applications, such as on-chip communications and sensing, microstrip-based structures remain highly relevant due to their low profile, ease of integration, and compatibility with CMOS technologies, as highlighted in the works of Jornet and Akyildiz[51] and Nagatsuma *et al.*[52].

3.3.2 Specific Absorption Rate (SAR)

SAR is a parameter used to quantify the amount of electromagnetic energy absorbed per unit mass of human tissue. It is defined in terms of power absorbed per unit mass and is expressed in watts per kilogram (W/kg). This indicator allows the level of penetration and deposition of electromagnetic energy in human tissue to be assessed, reflecting the speed at which the body absorbs energy when using wireless devices. THz waves have great potential for applications in spectroscopy, imaging, and biomedicine, mainly due to their ability to support high data transmission rates. However, as the wavelength decreases, there is a significant increase in free-space propagation loss, which poses additional challenges to the design and operation of these systems. One solution is to use high-gain antennas, which reduce interference effects and result in less radiation exposure to human tissues.

Thus, SAR constitutes a fundamental metric for evaluating human exposure to electromagnetic radiation, as widely discussed in the specialized literature[53–55]. However, as the wavelength decreases, there is a significant increase in free-space propagation loss, which poses additional challenges to the design and operation of these systems. One solution is to use high-gain antennas, which reduce interference effects and result in less radiation exposure to human tissues. Thus, SAR constitutes a fundamental metric for evaluating human exposure to electromagnetic radiation, as widely discussed in the specialized literature[53–55].

The SAR performance assessment was conducted using a multi-layer phantom model representative of human biological tissues. The interaction between the proposed antenna and the biological medium was simulated considering an equivalent phantom composed of three layers, corresponding to skin, fat, and muscle. Their electrical properties were adopted at the resonance frequencies (f_c) of the y-graphyne antennas, specifically at *3.28 THz*, *3.29 THz*, *3.52 THz*, and *3.59 THz* (see Table 3 for material parameters).

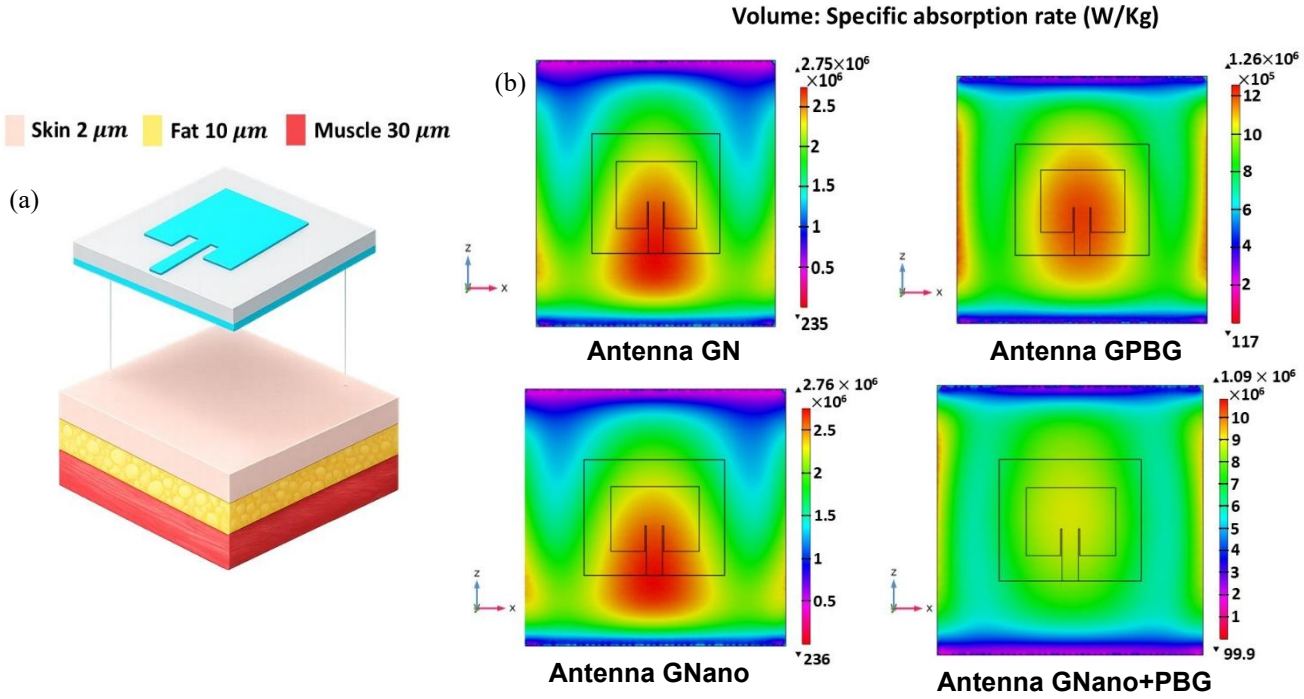


Figure 5. (a) Tissue equivalent three-layer phantom model, **(b)** SAR analysis tissue for microstrip antennas with *y- graphyne* patch via COMSOL software

Fig. 5(a) illustrates the simulation setup, which was performed in COMSOL Multiphysics, employing a 3D body phantom of *100 × 100 × 42 μm³*, suitable for analyzing electromagnetic absorption in THzband application.

The SAR performance of the proposed antenna was investigated using a biological tissue-equivalent phantom model, consisting of three distinct layers: skin (2 μm), fat (10 μm), and muscle (30 μm).The adopted 3D phantom has total dimensions of 100 × 100 × 42 μm³, while the antenna was positioned at a distance of 100 μm from the model's surface, aiming to reproduce operating conditions close to real electromagnetic exposure scenarios.

Fig. 5(b) presents the spatial distribution of the SAR considering an input power of *1 W*. It is observed that the highest maximum SAR value was obtained for the GN antenna operating at $f_c = 3.28$ THz, reaching 2.75×10^6 *W/kg*, while the GNano+PBG antenna presented the lowest value, equal to 1.09×10^6 *W/kg*. Despite the high absolute scale values, the obtained maximum SAR peak (2.75×10^6 *W/kg*) remains well below the permitted whole-body average exposure limit, ensuring that the emitted radiation does not pose a risk to human safety. The SAR values obtained in this work are consistent with the results reported by Azani and Zainal [53], who also evaluated electromagnetic exposure in the THz band. In that study, the authors registered a maximum SAR value of 2.49×10^6 *W/kg* and a minimum value of approximately 2.47×10^6 *W/kg*.

Table 4 presents the electrical properties of human tissues considered in this work. One of the main difficulties encountered during the research development was obtaining reliable data for the electromagnetic properties of tissues in the THz band. However, based on a literature analysis and grounded in the studies reported in references[54–57], the values presented in the aforementioned table were adopted.

Table 4 - Electrical Properties of Human Tissues in the proposed work.

Tissue	***f_c (THz)***	**Sigma 10^3 (S/m)**	**Permittivity (εr)**
Skin	*3.28*	1.8247	5.00
	3.52	1.8298	5.00
	3.29	1.9576	5.00
	3.59	1.9972	5.00
Fat	*3.28*	0.36495	2.50
	3.52	0.36608	2.50
	3.29	0.39138	2.50
	3.59	0.39939	2.50
Muscle	3.28	2.7370	6.00
	3.52	2.7493	6.00
	3.29	2.9384	6.00
	3.59	2.9958	6.00

4. Conclusion

This work connects atomistic predictions of γ-graphyne's electromagnetic response with device-level antenna design and demonstrates practical THz microstrip radiators by importing DFT plus Kubo derived surface conductivity into full-wave simulations. The multiscale procedure that combines first principles calculations and linear response modelling with finite element device simulation provides dispersive and realistic antenna predictions when experimental material data are not available. The surface conductivity data capture both interband features and scattering-dependent loss and these effects are shown to materially influence resonance frequency, input matching and radiation efficiency.

Simulated plain and edge-engineered patches resonate near 3.28 to 3.29 THz and exhibit deep matching with S11 below about −33 dB and bandwidths around 0.14 THz. Photonic bandgap based designs shift resonances to roughly 3.45 to 3.59 THz and produce the highest simulated peak gains of about 6.3 to 6.4 dB together with radiation efficiencies near 82 to 83 percent. Edge nanoribbons concentrate radiating currents and improve impedance matching without increasing footprint while PBG substrates reduce trapped substrate modes and raise gain and efficiency at the expense of increased sensitivity of the center frequency and feed impedance.

Convergence and sensitivity checks show that the identified performance trends are robust to reasonable variations in mesh parameters, scattering broadening and substrate permittivity, but that small lithographic errors at the percent level can shift the operating frequency by tens to hundreds of gigahertz in the THz band. For experimental progress it is important to obtain measured $\sigma(\omega)$ for realistic films and to pursue prototype fabrication with matched feeds and partial PBG implementations to ease manufacturability. Overall, γ-graphyne based microstrip patches evaluated through an atomistically informed workflow show a promising combination of miniaturization, matchability and radiation performance in the low THz band and merit further experimental validation.

Acknowledgments

D.H.C. thanks CAPES fellowship (Finance code 001). I.R.S.M thanks FACFIS/CANAN, LMMiLiE/PPGF and PPGF/UFPA. F.A.T.A. thanks PROPESP/UFPA. M.C.A.N. thanks ITEC/UFPA and PPGEE/UFPA. C.A.B. Silva Jr. thanks PROPESP/UFPA-PIBIC CNPq (PRO6735-2023) and CNPq (405727/2021-6 and 304459/2022-4). J.D.N. thanks CNPq (305064/2020-7 and 307567/2023-0) and UFPA-ICEN/PORTARIA Nº 303/2025 – COORDACADE.

References

1. Koppens FHL, Chang DE, García de Abajo FJ (2011) Graphene Plasmonics: A Platform for Strong Light–Matter Interactions. Nano Lett 11:3370–3377. https://doi.org/10.1021/nl201771h
2. Jablan M, Buljan H, Soljačić M (2009) Plasmonics in graphene at infrared frequencies. Phys Rev B 80:245435. https://doi.org/10.1103/PhysRevB.80.245435
3. Hanson GW (2008) Dyadic Green's functions and guided surface waves for a surface conductivity model of graphene. J Appl Phys 103:. https://doi.org/10.1063/1.2891452

4. Perruisseau-Carrier J (2012) Graphene for antenna applications: Opportunities and challenges from microwaves to THz. In: 2012 Loughborough Antennas & Propagation Conference (LAPC). IEEE, pp 1–4

5. D. Correas-Serrano and J. S. Gómez-Díaz Graphene-based antennas for terahertz systems: A review

6. Tamagnone M, Gómez-Díaz JS, Mosig JR, Perruisseau-Carrier J (2012) Analysis and design of terahertz antennas based on plasmonic resonant graphene sheets. J Appl Phys 112:. https://doi.org/10.1063/1.4768840

7. Tamagnone M, Gómez-Díaz JS, Mosig JR, Perruisseau-Carrier J (2012) Reconfigurable terahertz plasmonic antenna concept using a graphene stack. Appl Phys Lett 101:. https://doi.org/10.1063/1.4767338

8. Greenwood DA (1958) The Boltzmann Equation in the Theory of Electrical Conduction in Metals. Proceedings of the Physical Society 71:585–596. https://doi.org/10.1088/0370-1328/71/4/306

9. Jia Z, Li Y, Zuo Z, et al (2017) Synthesis and Properties of 2D Carbon—Graphdiyne. Acc Chem Res 50:2470–2478. https://doi.org/10.1021/acs.accounts.7b00205

10. Gao X, Liu H, Wang D, Zhang J (2019) Graphdiyne: synthesis, properties, and applications. Chem Soc Rev 48:908–936. https://doi.org/10.1039/C8CS00773J

11. Ivanovskii AL (2013) Graphynes and graphdyines. Progress in Solid State Chemistry 41:1–19. https://doi.org/10.1016/j.progsolidstchem.2012.12.001

12. Desyatkin VG, Martin WB, Aliev AE, et al (2022) Scalable Synthesis and Characterization of Multilayer γ-Graphyne, New Carbon Crystals with a Small Direct Band Gap. J Am Chem Soc 144:17999–18008. https://doi.org/10.1021/jacs.2c06583

13. Kang J, Wei Z, Li J (2019) Graphyne and Its Family: Recent Theoretical Advances. ACS Appl Mater Interfaces 11:2692–2706. https://doi.org/10.1021/acsami.8b03338

14. Hou X, Xie Z, Li C, et al (2018) Study of Electronic Structure, Thermal Conductivity, Elastic and Optical Properties of α, β, γ-Graphyne. Materials 11:188. https://doi.org/10.3390/ma11020188

15. Pitarke JM, Silkin VM, Chulkov E V, Echenique PM (2007) Theory of surface plasmons and surface-plasmon polaritons. Reports on Progress in Physics 70:1–87. https://doi.org/10.1088/0034-4885/70/1/R01

16. Gómez-Díaz JS, Perruisseau-Carrier J (2012) Propagation of hybrid transverse magnetic-transverse electric plasmons on magnetically biased graphene sheets. J Appl Phys 112:. https://doi.org/10.1063/1.4769749

17. Huang X, Leng T, Zhu M, et al (2015) Highly Flexible and Conductive Printed Graphene for Wireless Wearable Communications Applications. Sci Rep 5:18298. https://doi.org/10.1038/srep18298

18. Soler JM, Artacho E, Gale JD, et al (2002) The SIESTA method for *ab initio* order- *N* materials simulation. Journal of Physics: Condensed Matter 14:2745–2779. https://doi.org/10.1088/0953-8984/14/11/302

19. Castro Neto AH, Guinea F, Peres NMR, et al (2009) The electronic properties of graphene. Rev Mod Phys 81:109–162. https://doi.org/10.1103/RevModPhys.81.109

20. Perdew JP, Burke K, Ernzerhof M (1996) Generalized Gradient Approximation Made Simple. Phys Rev Lett 77:3865–3868. https://doi.org/10.1103/PhysRevLett.77.3865

21. García A, Papior N, Akhtar A, et al (2020) SIESTA: Recent Developments and Applications. J Chem Phys 152:. https://doi.org/10.1063/5.0005077

22. Kubo R (1957) Statistical-Mechanical Theory of Irreversible Processes. I. General Theory and Simple Applications to Magnetic and Conduction Problems. J Physical Soc Japan 12:570–586. https://doi.org/10.1143/JPSJ.12.570

23. Calderín L, Karasiev VV, Trickey SB (2017) Kubo–Greenwood electrical conductivity formulation and implementation for projector augmented wave datasets. Comput Phys Commun 221:118–142. https://doi.org/10.1016/j.cpc.2017.08.008

24. García de Abajo FJ (2014) Graphene Plasmonics: Challenges and Opportunities. ACS Photonics 1:135–152. https://doi.org/10.1021/ph400147y

25. Bludov YU V., Ferreira A, Peres NMR, vasilevskiy mi (2013) a primer on surface plasmon-polaritons in graphene. Int J Mod Phys B 27:1341001. https://doi.org/10.1142/S0217979213410014

26. Sampaio-Silva A, Ferreira DF, Silva CAB, Del Nero J (2022) Hydrogenation, width and strain effect in Me-graphene devices. Comput Mater Sci 210:111456. https://doi.org/10.1016/j.commatsci.2022.111456

27. Mikhailov SA (2011) Theory of the giant plasmon-enhanced second-harmonic generation in graphene and semiconductor two-dimensional electron systems. Phys Rev B 84:045432. https://doi.org/10.1103/PhysRevB.84.045432

28. El Misilmani HM, Al-Husseini M (2019) 1D Slotted Waveguide Antenna with Controlled Beamwidth and Sidelobe Level Ratio. In: 2019 IEEE International Symposium on Antennas and Propagation and USNC-URSI Radio Science Meeting. IEEE, pp 1421–1422

29. Dmitriev V, Rodrigues NRNM, de Oliveira RMS, Paiva RR (2021) Graphene Rectangular Loop Antenna for Terahertz Communications. IEEE Trans Antennas Propag 69:3063–3073. https://doi.org/10.1109/TAP.2020.3030991

30. Dong Y, Liu P, Yu D, et al (2016) Dual-Band Reconfigurable Terahertz Patch Antenna With Graphene-Stack-Based Backing Cavity. IEEE Antennas Wirel Propag Lett 15:1541–1544. https://doi.org/10.1109/LAWP.2016.2533018

31. Y. Qian RCDSVREY and TI (1999) A microstrip patch antenna using novel photonic band-gap structures. Microw J (Int Ed) 42:66–76

32. Llatser I, Kremers C, Cabellos-Aparicio A, et al (2012) Graphene-based nano-patch antenna for terahertz radiation. Photonics Nanostruct 10:353–358. https://doi.org/10.1016/j.photonics.2012.05.011

33. Kumar C, Raghuwanshi SK, Kumar S (2024) Graphene-based terahertz antenna on a photonic band gap substrate: design, analysis, and performance evaluation for optical applications. In: Sadwick LP, Yang T (eds) Terahertz, RF, Millimeter, and Submillimeter-Wave Technology and Applications XVII. SPIE, p 65

34. Correas-Serrano D, Gomez-Diaz JS, Alvarez-Melcon A (2014) On the Influence of Spatial Dispersion on the Performance of Graphene-Based Plasmonic Devices. https://doi.org/10.1109/LAWP.2014.2305836

35. Thongrattanasiri S, Koppens FHL, García de Abajo FJ (2012) Complete Optical Absorption in Periodically Patterned Graphene. Phys Rev Lett 108:047401. https://doi.org/10.1103/PhysRevLett.108.047401

36. Pan L, Zhang L, Song B, et al (2012) Graphyne- and Graphdiyne-based Nanoribbons: Density Functional Theory Calculations of Electronic Structures. https://doi.org/10.1063/1.3583507

37. Asadpour M, Jafari M, Asadpour M, Jafari M (2015) Optical properties of two-dimensional zigzag and armchair graphyne nanoribbon semiconductor. Spectrochim Acta A Mol Biomol Spectrosc 139:380–384. https://doi.org/10.1016/j.saa.2014.12.020

38. Chang CC, Qian Y, Itoh T (2003) analysis and applications of uniplanar compact photonic bandgap structures. Progress In Electromagnetics Research, 41, 211-235. doi:10.2528/PIER06081501.

39. Temmar MNE, Hocini A, Khedrouche D, Zamani M (2019) Analysis and design of a terahertz microstrip antenna based on a synthesized photonic bandgap substrate using BPSO. J Comput Electron 18:231–240. https://doi.org/10.1007/s10825-019-01301-x

40. C. A. Balanis (2016) Antenna theory: analysis and design., 4th ed. John wiley & sons

41. Yadav R, Gotra S, Pandey VS, Kumar S (2023) Graphene based two-port MIMO yagi-uda antenna for THz applications. Micro and Nanostructures 181:207616. https://doi.org/10.1016/j.micrna.2023.207616

42. Yadav R, Pandey VS, Verma P (2024) Nano-Scaled Graphene Plasmonic-Based Vanadium Dioxide Yagi-Uda Array MIMO Antenna for Terahertz Applications. Plasmonics 19:3345–3358. https://doi.org/10.1007/s11468-024-02239-y

43. Pant R, Malviya L (2023) THz antennas design, developments, challenges, and applications: A review. International Journal of Communication Systems 36:. https://doi.org/10.1002/dac.5474

44. Joler M, Mihalić L (2022) A Subtlety of Sizing the Inset Gap Width of a Microstrip Antenna When Built on an Ultra-Thin Substrate in the S-Band. Sensors 23:213. https://doi.org/10.3390/s23010213

45. Tripathi SK, Kumar A (2021) Performance Comparison of Graphene Terahertz Antenna and Copper Terahertz Antenna. pp 489–497

46. Paul LC, Islam MdM (2017) Proposal of wide bandwidth and very miniaturized having dimension of μm range slotted patch THz microstrip antenna using PBG substrate and DGS. In: 2017 20th International Conference of Computer and Information Technology (ICCIT). IEEE, pp 1–6

47. Bala R, Marwaha A (2016) Development of computational model for tunable characteristics of graphene based triangular patch antenna in THz regime. J Comput Electron 15:222–227. https://doi.org/10.1007/s10825-015-0761-6

48. George S, Vijayakumar N (2022) Investigations of Substrate and Patch Materials for Sub-Terahertz Wireless Applications Scenario. J Electron Mater 51:5065–5073. https://doi.org/10.1007/s11664-022-09734-0

49. Anand S, Sriram Kumar D, Wu RJ, Chavali M (2014) Graphene nanoribbon based terahertz antenna on polyimide substrate. Optik (Stuttg) 125:5546–5549. https://doi.org/10.1016/j.ijleo.2014.06.085

50. Jeyakumar P, Anandpushparaj J, Thanapal P, et al (2023) Terahertz Micro-Strip Patch Antenna Design and Modelling for 6G Mobile Communication. Journal of Electrical Engineering & Technology 18:2253–2262. https://doi.org/10.1007/s42835-022-01308-8

51. Josep Miquel Jornet; Ian F. Akyildiz (2010) Graphene-based nano-antennas for electromagnetic nanocommunications in the terahertz band. Proceedings of the European Conference on Antennas and Propagation 1–5

52. Nagatsuma T, Ducournau G, Renaud CC (2016) Advances in terahertz communications accelerated by photonics. Nat Photonics 10:371–379. https://doi.org/10.1038/nphoton.2016.65

53. Md Azani MAS, Zainal Abidin Z (2023) Terahertz Microstrip Patch Antenna for Breast Tumour Detection. Journal of Electronic Voltage and Application 4:. https://doi.org/10.30880/jeva.2023.04.01.006

54. Vilagosh Z, Lajevardipour A, Wood AW (2020) Computational absorption and reflection studies of normal human skin at 0.45 THz. Biomed Opt Express 11:417. https://doi.org/10.1364/BOE.377424

55. Jördens C, Scheller M, Breitenstein B, et al (2009) Evaluation of leaf water status by means of permittivity at terahertz frequencies. J Biol Phys 35:255–264. https://doi.org/10.1007/s10867-009-9161-0

56. Ney M, Abdulhalim I (2011) Modeling of reflectometric and ellipsometric spectra from the skin in the terahertz and submillimeter waves region. J Biomed Opt 16:067006. https://doi.org/10.1117/1.3592779

57. Lajevardipour A, Wood AW, McIntosh RL, Iskra S (2016) Estimation of dielectric values for tissue water in the Terahertz range. Bioelectromagnetics 37:563–567. https://doi.org/10.1002/bem.22010